Imaging protein three-dimensional nanocrystals with cryo-EM

Nederlof, I.; Li, YW.; Heel, M.G. van; Abrahams, J.P.

Imaging protein three-dimensional nanocrystals with cryo-EM

**Igor Nederlof, Yao Wang Li,
Marin van Heel and Jan Pieter
Abrahams***

Leiden Institute of Chemistry, Leiden University,
Einsteinweg 55, 2333 CC Leiden, The
Netherlands

Correspondence e-mail:
abrahams@chem.leidenuniv.nl

Flash-cooled three-dimensional crystals of the small protein lysozyme with a thickness of the order of 100 nm were imaged by 300 kV cryo-EM on a Falcon direct electron detector. The images were taken close to focus and to the eye appeared devoid of contrast. Fourier transforms of the images revealed the reciprocal lattice up to 3 Å resolution in favourable cases and up to 4 Å resolution for about half the crystals. The reciprocal-lattice spots showed structure, indicating that the ordering of the crystals was not uniform. Data processing revealed details at higher than 2 Å resolution and indicated the presence of multiple mosaic blocks within the crystal which could be separately processed. The prospects for full three-dimensional structure determination by electron imaging of protein three-dimensional nanocrystals are discussed.

1. Introduction

Three-dimensional protein crystals that are smaller than about 1 µm are beyond the scope of the usual diffraction methods in structural biology. Since about 30% of proteins that crystallize do not produce crystals of a sufficient size or quality for X-ray structure determination (Rupp, 2004; Quevillon-Cheruel *et al.*, 2004), this is a serious bottleneck. Structural information on important drug targets, such as membrane proteins and large complexes, is often lacking owing to the inability to grow sufficiently sized and ordered crystals. Current trends in X-ray crystallography focus on data collection from ever smaller crystals. For example, micro-focused X-ray beams and improved quantum area detectors, such as the PILATUS, have decreased the size limits on crystals (Cusack *et al.*, 1998; Eikenberry *et al.*, 2003). In particular, free-electron lasers expand the crystallographic method towards smaller crystals (Chapman *et al.*, 2011). We believe that electron microscopy could have a large impact on the field of protein nanocrystallography since electrons are several orders of magnitude less damaging to protein crystals than X-rays per diffracted quantum (Henderson, 1995).

Since the development of cryo-electron microscopy (cryo-EM) and macromolecular reconstructions in the 1970s (Taylor & Glaeser, 1974; Klug, 1979; Knapek & Dubochet, 1980), there have been constant improvements in the maximum resolution that can be achieved using this method. Recent advances in 'single-particle analysis' make the solution of large molecular complexes at atomic resolution imminent (van Heel *et al.*, 2000; Zhou, 2008). Important recent improvements in single-particle analysis have been automated sample handling (FEI EPU; http://investor.fei.com/releasedetail.cfm?ReleaseID=495245; Carragher *et al.*, 2000), automated image processing (van Heel *et al.*, 1996, 2012; Tang *et al.*, 2007) and

direct electron detection (FEI Falcon; http://investor.fei.com/releasedetail.cfm?ReleaseID=399045; Llopart Cudié *et al.*, 2002). Automated data collection makes it possible to collect millions of images and software can automatically average the signal and perform angular reconstructions of the protein models. Beam damage can be minimized by using efficient direct electron detectors which significantly improve the signal-to-noise ratio at low electron-dose conditions.

In material sciences, electron diffraction is a well developed tool for structure determination of inorganic crystals, in which selected area electron diffraction from different zone axes can be used to determine three-dimensional unit cells. Convergent-beam electron diffraction (Spence & Zuo, 1992) can be used to obtain more information about the symmetry of the crystal. The development of precession electron diffraction (Vincent & Midgley, 1994; Oleynikov *et al.*, 2007), automated diffraction tomography (Kolb *et al.*, 2007; Mugnaioli *et al.*, 2009) and rotation electron diffraction (Zhang *et al.*, 2010) have contributed to the toolbox of electron crystallographers. Applications for electron crystallography of small molecules are becoming robust, making three-dimensional structure determination by electron diffraction of three-dimensional nanocrystals a very attractive method.

Structure determination using electron diffraction of two-dimensional protein crystals has been used since the seminal work on bacteriorhodopsin in the 1970s (Henderson & Unwin, 1975). In 2005, the structure of two-dimensional aquaporin crystals was solved to a resolution of 1.9 Å (Gonen *et al.*, 2005). However, three-dimensional nanocrystals of proteins have so far resisted structure determination. The main reasons for this are the beam sensitivity, the large unit cell and the thickness of the crystals. The latter factor contributes to increased multiple scattering and nonlinear effects in electron diffraction and imaging. However, multi-slice least-squares methods (Jansen *et al.*, 1998) have tackled such problems in electron crystallography of small molecules. To increase the
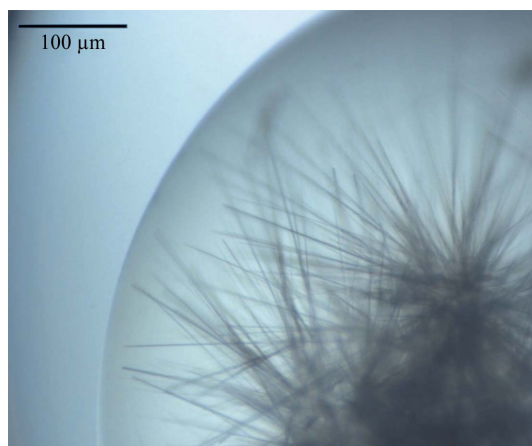
resolution and refine structural models, electron-diffraction data can be combined with electron-microscopy images, which contain phase information (Henderson & Unwin, 1975; Weirich *et al.*, 2000; Tsuda & Tanaka, 1995; Zuo & Spence, 1991). Phases from these electron microgrms can also be used to solve structures from X-ray diffraction where phases are missing (Dodson, 2001; Navaza, 2008).

Here, we report the electron imaging of three-dimensional protein nanocrystals that were prepared using standard protein-crystallization techniques. We have previously collected rotation electron-diffraction data of similar lysozyme nanocrystals to a resolution of 1.8 Å (Nederlof *et al.*, 2013). We discuss the preliminary image-processing results and the possibility of integrating diffraction data with imaging data.

2. Materials and methods

2.1. Crystallization

Crystallization experiments were carried out using the standard sitting-drop vapour-diffusion technique in Innovadyne SD-2 plates. The *Rock Maker* software (Formulatrix) was used to design the experiments. We used a Genesis (Tecan) to dispense the screening solutions into the reservoirs. An Oryx 6 crystallization robot (Douglas Instruments) was used to transfer 500 nl reservoir solution and 500 nl protein solu-
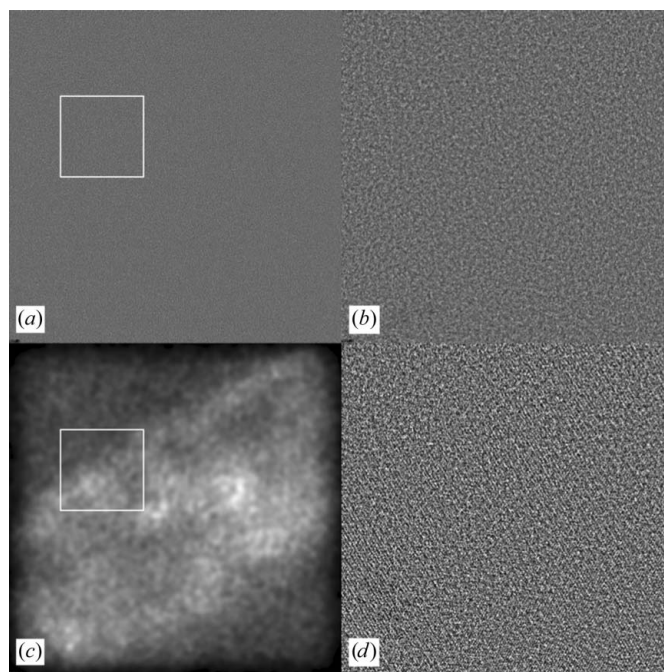

Figure 1
Lysozyme nanocrystals in a crystallization drop imaged with a light microscope. The needle-shaped crystals that are visible under the light microscope are too thick for EM analysis because of absorption. However, the crystallization drops also contain (much) smaller crystals with a thickness of the order of 100 nm, which could be imaged at high resolution by cryo-EM.

Figure 2
(*a*) An electron micrograph of a lysozyme three-dimensional nanocrystal collected using a Titan cryo-EM with a Falcon camera (4096 × 4096 pixels, 0.9 Å per pixel). The location of the enlargement shown in (*b*) is indicated. (*b*) Enlargement (1024 × 1024 pixels) of (*a*). Although appearing to be just noise, the image shown here in fact does contain very significant high-resolution detail, as is revealed by its Fourier transform (Fig. 3). Calculating the local variance of the lattice-enhanced image within a circular area with a diameter of 30 pixels reveals the shape of the crystal (*c*). A Wiener filter can be used to enhance the lattice contrast, as shown in (*d*), which is equivalent to (*b*) after filtering.
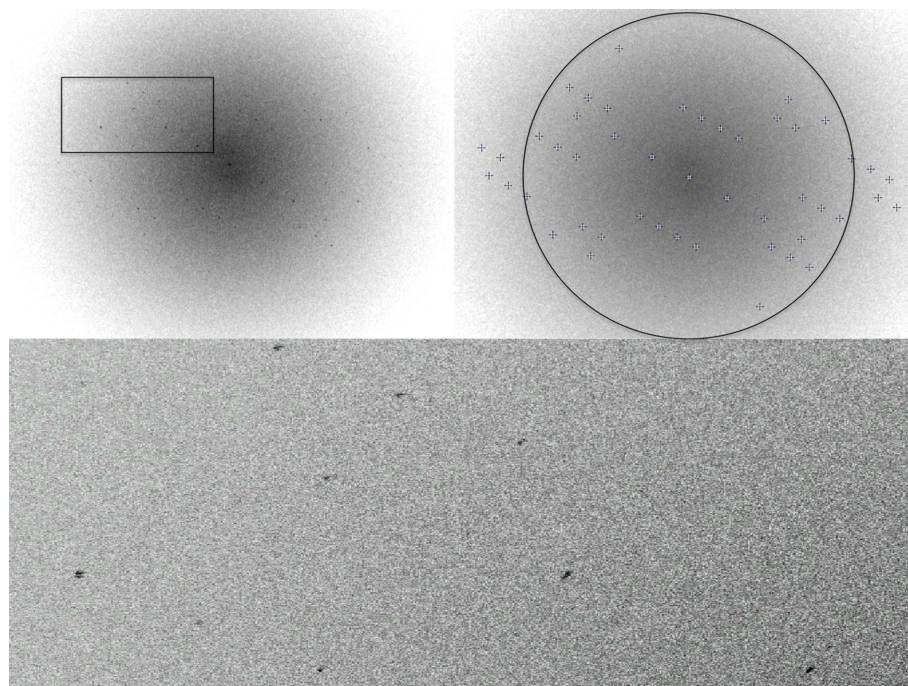
Figure 3
Top left, slightly enlarged Fourier transform of Fig. 2(*a*). Top right, Fourier transform of Fig. 2, with peak positions indicated, showing a projection of a regular three-dimensional lattice (the ring represents 4.5 Å). Bottom, detail of the top left, showing the structure of the Bragg spots.
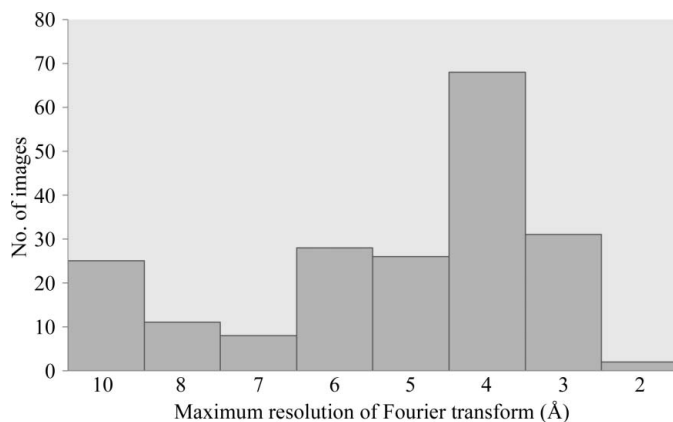

Figure 4
Histogram of the maximum resolution observed in electron images of 200 different lysozyme three-dimensional nanocrystals.

tion into sitting-drop wells. The plates were stored at 293 K and imaged using the Rock Imager automated imaging system (Formulatrix). Lysozyme (8 mg ml^{-1}) formed needle-shaped crystals after 48 h when mixed in a 1:1 ratio with well solution consisting of 0.1 *M* sodium acetate pH 3.8, 1.0 *M* potassium nitrate (Fig. 1).

2.2. Vitrification

Protein crystals were vitrified using a Vitrobot (FEI; http://investor.fei.com/releasedetail.cfm?ReleaseID=255249; Frederik & Hubert, 2005). 3 µl well solution was mixed with the drop containing nanocrystals and transferred onto a 3 mm

holey carbon grid (Agar). Excess liquid was blotted away (blot time 3 s; blot force 5) and the sample was plunge-frozen in liquid ethane. Samples were transferred into the microscope immediately and loaded and kept at 93 K using an automated cryo-loader/cryo-stage.

2.3. Electron-microscopy data collection

Electron images were obtained using a Titan Krios (FEI) transmission electron microscope at NeCEN. The FEG was operated at 300 keV and a Falcon (FEI) 4k × 4k direct electron detector was used at 0.822 and 1.055 Å per pixel. The electron dose used was between 5 and 10 e$^-$ Å^{-2}.

3. Results

Image data were collected from about 200 lysozyme three-dimensional nanocrystals in random orientations and at tilt angles varying between −45 and +45°. All images were collected close to the Scherzer focus (which is ∼70 nm at 300 kV) and were devoid of amplitude contrast (Fig. 2). However, Fourier transformation of the images indicated crystalline order (Fig. 3), with discernable Bragg spots extending to about 4 Å or better for about half of the crystals and even further in favourable cases (Fig. 4). The crystals that yielded the best resolution on average were about 100 nm thick, as determined by tomography (Fig. 5). We did not orient the crystals prior to high-resolution imaging, so most of their Fourier transforms showed multiple Laue zones (Fig. 3). These multiple Laue zones appeared as two-dimensional lattices of Bragg spots with three primitive spacings; the third spacing corresponds to the distance between lunes that are observed in diffraction patterns. This is different from two-dimensional electron crystallography, as diffraction patterns of two-dimensional protein crystals only have two primitive spacings. The presence of three primitive spacings predictably leads to moiré patterns in the real-space image. The repeat of this complex pattern of fringes that is caused by the multiple Laue zones is determined by the smallest common denominator between the primitive spacings.

3.1. Structure of the Bragg spots

Detailed analysis revealed the Bragg peaks to be structured (Fig. 3). In diffraction studies, the shape (but not the intensity) of a Bragg peak is the product of the shape of the source and the variation of the crystal spacing corresponding to the index of the Bragg peak within the diffracting crystal. As we did not measure the diffraction pattern, but instead calculated the

Fourier transform of an EM image, the situation was slightly different. The shape of the source turned out to be irrelevant. The observed structure of the Bragg peaks must therefore at least in part be caused by the shape and internal ordering of the crystal. In some cases splitting of the diffraction spots was observed (*e.g.* the leftmost spot in the bottom part of Fig. 3), but splitting was by no means the norm. Like the other irregularities in the Bragg spots, splitting could be caused by non-uniform ordering of the crystal, but Ewald sphere curvature cannot be ruled out as a contributing factor, as explained in §4.

By Fourier transforming the images, we could not only calculate the intensity distribution within the Bragg spots, but also the phases of each reciprocal pixel. Using *ImageJ* (Abramoff *et al.*, 2004), both the intensity and the phase of each reciprocal pixel can be inspected in a number field. Inspection showed that the phase correlation between adjacent reciprocal pixels was low within a single Bragg spot. This suggests that the observed spreading of the Bragg spots was probably caused by local differences in the size and projected potential of the unit cells (resulting in subtle origin shifts of the unit cells with respect to the average lattice), rather than by in-plane rotations of unit cells relative to one another (which would have preserved the phase).

3.2. Centrosymmetry of the Fourier transform

A detector placed in the diffraction plane of the microscope measures a diffraction pattern. Its intensities are those of the Fourier $F(\mathbf{h})$ of the electron-plane-wave-function $\psi_e(\mathbf{x})$ that has passed through the sample,

$$F(\mathbf{h}) = \mathbf{F}^{-1}[\psi_e(\mathbf{x})]. \qquad (1)$$

This Fourier transform of the exit wavefunction $\psi_e(\mathbf{x})$ peaks at the Bragg positions determined by the periodicity of the crystal. In imaging mode, the lenses of the microscope recombine these structure factors through a Fourier transform into a real-space defocused electron-plane wavefunction $\psi_{\Delta f}(\mathbf{x})$. Distortions of this recombination are described by a centrosymmetric transfer function $\tau(\mathbf{h})$, which is determined by the wavelength of the electrons, aberrations of the electron lenses and the defocus (the coherence of the illumination system and the position of the detector relative to the focal imaging plane of the microscope),

$$\psi_{\Delta f}(\mathbf{x}) = \mathbf{F}[F(\mathbf{h})\tau(\mathbf{h})]. \qquad (2)$$

Note that $\psi_{\Delta f}(\mathbf{x})$ is a complex wavefunction. When $\psi_{\Delta f}(\mathbf{x})$ impinges on the detector, the wavefunction collapses and its intensities [which are calculated by multiplying $\psi_{\Delta f}(\mathbf{x})$ by its
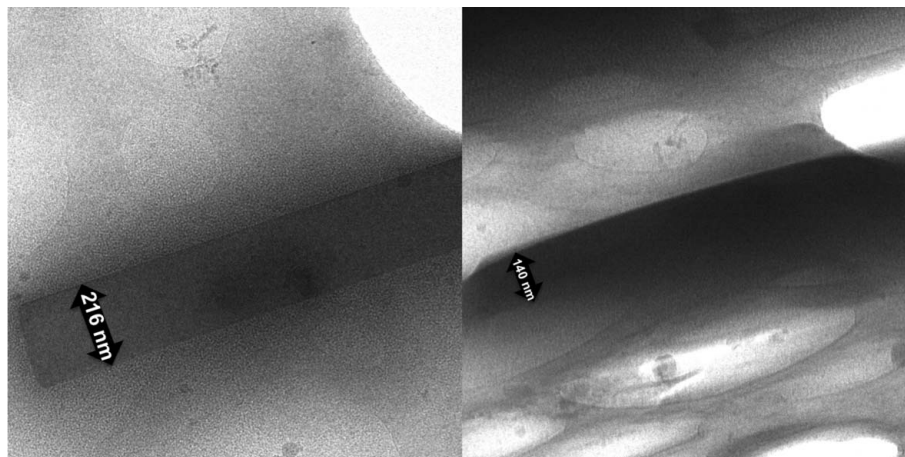

Figure 5
Two defocused (−8.00 µm) frames from raw data of a tomographic series of one of the crystals from which the high-resolution data were collected. Frames were taken at 0° (left) and at 44° (right) and show that the crystal was less than 150 nm thick.
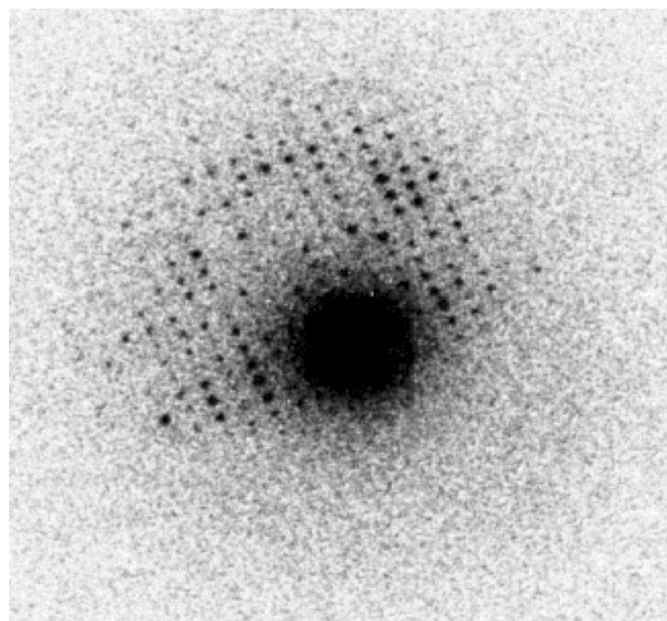

Figure 6
Electron diffraction pattern showing lunes (at 200 keV).

complex conjugate $\overline{\psi_{\Delta f}(\mathbf{x})}$] are measured as the electron image $M(\mathbf{x})$,

$$M(\mathbf{x}) = \psi_{\Delta f}(\mathbf{x})\overline{\psi_{\Delta f}(\mathbf{x})}. \qquad (3)$$

Note that $M(\mathbf{x})$ is a real function, so its Fourier transform $\mathbf{F}^{-1}[M(\mathbf{x})]$ must obey Hermitian symmetry: $\mathbf{F}^{-1}[M(\mathbf{x})] = \overline{\mathbf{F}^{-1}[M(-\mathbf{x})]}$. However, in the general case $F(\mathbf{h})$ is not centrosymmetric. Hence, the Fourier transform of the measured image cannot be equivalent to $F(\mathbf{h})\tau(\mathbf{h})$. An example of a typical electron-diffraction pattern of a non-oriented lysozyme three-dimensional nanocrystal is shown in Fig. 6. The curvature of the Ewald sphere, in combination with the parallel electron beam, causes the Bragg spots to be

limited to the so-called lunes that are such a usual and prominent feature in X-ray diffraction patterns of non-oriented protein crystals. These lunes clearly break centro-symmetry.

Nevertheless, even though the crystallographic phases corrected by $\tau(\mathbf{h})$ are not necessarily always equivalent to the phases of $\mathbf{F}^{-1}[M(\mathbf{x})]$, it is possible (through iterative procedures) to retrieve crystallographic phase information from the inverse Fourier transform of $M(\mathbf{x})$. This is relatively straightforward if the weak phase object approximation holds. Firstly, we have to realise that the Fourier transform of $M(\mathbf{x})$ is equivalent to the autocorrelation of the Fourier transform of $\psi_{\Delta f}(\mathbf{x})$. This follows from the convolution theorem,

$$\mathbf{F}^{-1}[M(\mathbf{x})] = \int F_{\Delta f}(\mathbf{h}_t) F_{\Delta f}(\mathbf{h} + \mathbf{h}_t)\, \mathrm{d}\mathbf{h}_t. \qquad (4)$$

The weak phase object approximation implies that most of the power of $F_{\Delta f}(\mathbf{h})$ is located at $\mathbf{h} = \mathbf{0}$. This implies that we can use the following approximation for weak phase objects,

$$F_{\Delta f}(\mathbf{h}_t) F_{\Delta f}(\mathbf{h} + \mathbf{h}_t) \neq 0 \;\Rightarrow\; \mathbf{h}_t = \mathbf{0} \;\vee\; \mathbf{h} + \mathbf{h}_t = \mathbf{0}. \qquad (5)$$

Therefore, the product $F_{\Delta f}(\mathbf{h}_t) F_{\Delta f}(\mathbf{h} + \mathbf{h}_t)$ is only nonzero if either $\mathbf{h}_t = \mathbf{0}$ and/or if $\mathbf{h} + \mathbf{h}_t = \mathbf{0}$. Using this restriction, the integral in lemma (4) can be simplified, as $\mathbf{h}_t$ can be substituted by $\mathbf{0}$ or $-\mathbf{h}$,

$$\mathbf{F}^{-1}[M(\mathbf{x})] = \int \overline{F_{\Delta f}(\mathbf{0})} F_{\Delta f}(\mathbf{h}) + \overline{F_{\Delta f}(-\mathbf{h})} F_{\Delta f}(\mathbf{0})\, \mathrm{d}\mathbf{h}_t. \qquad (6)$$

This reduces to

$$\frac{\mathbf{F}^{-1}[M(\mathbf{x})]}{F_{\Delta f}(\mathbf{0})} = F_{\Delta f}(\mathbf{h}) + \overline{F_{\Delta f}(-\mathbf{h})}. \qquad (7)$$

In other words, provided that the weak phase object approximation holds, the reverse Fourier transform of the measured image is the same as the defocused set of structure factors of the crystal (in any orientation) added to the complex complement of the same set after a point inversion through the origin (which is equivalent to a rotation by) followed by taking the complex complement.

The implications of this conjecture are as follows.

(i) The reverse Fourier transform of the measured image has Friedel symmetry (which is another way of saying that the measured image is real).

(ii) The amplitude of a structure factor is affected provided that the diffraction pattern (rather than the inverse Fourier transform of the image) does not have another structure factor located at the location after a rotation about the centre by π.

(iii) If the diffraction pattern records two Friedel mates simultaneously, the amplitude of these reflections in the inverse transform of the measured image is changed, but the phase is not affected.

(iv) If the diffraction pattern records two Friedel mates simultaneously but only partially (owing to the presence of mosaic blocks, for instance), splitting can occur if the two reflections are not recorded on spot-on centrosymmetric locations.

(v) If the diffraction pattern records two reflections that are not Friedel mates but that occur by chance at each other's centrosymmetric locations, the reverse transform of the image mixes the two by adding one to the complex complement of the other, thus imposing Hermitian symmetry on the reverse transform.

(vi) Because of the imposition of centrosymmetry on the reverse transform, information on the handedness is lost.

Similar considerations, albeit in different formalisms, have been discussed in papers on the implications of the curvature of the Ewald sphere on single-particle reconstructions (Wolf et al., 2006) and in two-dimensional crystallography (Philippsen et al., 2007). There are also parallels with the single-sideband approach in electron microscopy (Hohenstein, 1992).

3.3. Visualizing the lattice

The translational symmetry of an EM image of a (three-dimensional) nanocrystal can be enhanced by first Fourier transforming the image, then zeroing all reciprocal pixels that do not belong to the lattice and finally reversing the Fourier transform. This procedure has been applied with great success in two-dimensional protein crystallography (see, for example, Henderson & Unwin, 1975). We can enhance this procedure by assuming that the signal of the crystal lattice is not correlated with the noise. This implies a phase difference of $\pi/2$ between the expected structure factors of the lattice on the one hand and noise on the other. This implies[1]

$$|F_{\mathrm{m}}(\mathbf{h})|^2 = |\langle F_{\mathrm{l}}(\mathbf{h})\rangle|^2 + |\langle F_{\mathrm{n}}(\mathbf{h})\rangle|^2. \qquad (8)$$

The phase of $F_{\mathrm{m}}(\mathbf{h})$ is the best (and only) estimate of the phase of $F_{\mathrm{l}}(\mathbf{h})$. We therefore have to project $F_{\mathrm{l}}(\mathbf{h})$ onto $F_{\mathrm{m}}(\mathbf{h})$ to obtain the best estimate of the structure factor corresponding to the lattice, denoted here by $F_{\mathrm{W,l}}(\mathbf{h})$. The right-angled geometry that imposed lemma (8) also implies

$$F_{\mathrm{W,l}}(\mathbf{h}) = F_{\mathrm{m}}(\mathbf{h}) \frac{|\langle F_{\mathrm{l}}(\mathbf{h})\rangle|^2}{|F_{\mathrm{m}}(\mathbf{h})|^2}. \qquad (9)$$

Substitution with (8) results in

$$F_{\mathrm{W,l}}(\mathbf{h}) = F_{\mathrm{m}}(\mathbf{h})\left[1 - \frac{|\langle F_{\mathrm{n}}(\mathbf{h})\rangle|^2}{|F_{\mathrm{m}}(\mathbf{h})|^2}\right]. \qquad (10)$$

This is equivalent to an optimal (Wiener) filter, which requires calculation of the ratio between an estimate of the power spectrum of the noise $|\langle F_{\mathrm{n}}(\mathbf{h})\rangle|^2$ and the smoothed power spectrum of the measured image $|F_{\mathrm{m}}(\mathbf{h})|^2$ (Press et al., 2007). We generated this optimal lattice filter by first smoothing the power spectrum of the image using a soft-edged circular window with a radius of 256 reciprocal pixels. We estimated the power spectrum of the noise to be the rotational average of this smoothed power spectrum. In order to prevent $F_{\mathrm{m}}(\mathbf{h})$ being multiplied by negative numbers in (10), we applied a threshold limiting the range of its scale factor to (0, 1). The application of (10) clearly revealed the lattice (Fig. 2c). The

---

[1] For each reciprocal pixel $\mathbf{h}$, we define $F_{\mathrm{m}}(\mathbf{h})$ to be the measured structure factor and $|F_{\mathrm{m}}(\mathbf{h})|$ is its amplitude; $|\langle F_{\mathrm{l}}(\mathbf{h})\rangle|$ is the amplitude of the expected structure factor of the lattice and $|\langle F_{\mathrm{n}}(\mathbf{h})\rangle|$ is the amplitude of the expected structure factor of the noise.

outline of the crystal now becomes apparent on calculating the local variance of the lattice-enhanced image (Fig. 2d).

Further image processing with *IMAGIC* (van Heel *et al.*, 2012) enhanced the resolution. We randomly picked 101 patches of 256 × 256 pixels from the lattice-enhanced image, aligned them and classified them (van Heel *et al.*, 1989) into three classes (Fig. 7, top panel). We used these classes to identify 4500 equivalent patches in the lattice-enhanced image by a correlation search. The locations with high correlation were in agreement with the contour of the nanocrystal (compare Fig. 2d with the top right panel of Fig. 7).

We classified the selected patches into five different classes of on average 900 patches. Four of the class averages are shown in the second panel from the top in Fig. 7. A fifth class

that had less pronounced contrast and was located at the edges of the crystal is not shown.

The resolution of the patch averages is illustrated using their Fourier transforms (the second panel from the bottom in Fig. 7). At lower contour levels, spots can be seen extending almost to the Nyquist frequency (1.64 Å). The classes differ both in real space and in reciprocal space. In reciprocal space, Bragg spots that are prominent in one amplitude spectrum are hardly visible in the other amplitude spectra and *vice versa*. These differences in reciprocal space are not resolution-dependent. Notice furthermore that the differences between classes 1 and 2 and between classes 3 and 4 are subtle, but that the differences between classes 1 and 4 are more pronounced.

We analysed all crystals from which we collected images that showed Bragg spots beyond 4 Å resolution. All resulted in high-resolution, high-contrast classes, some of which are shown in Fig. 8.

4. Discussion and conclusions

We have shown that three-dimensional protein nanocrystals that are too small for conventional (synchrotron) X-ray analysis can be robustly imaged at high resolution with electrons. Fourier transforms of these images reveal the presence of moiré lattices caused by interference between the lattices of the zero-order Laue zone with higher order Laue zones, indicating that the crystals are not aligned with their principal axes parallel to the electron beam. Furthermore, the Fourier transforms have Hermitian symmetry, which has some repercussions for extracting crystallographic phase information. As long as the weak phase object approximation is valid (which is the case when most electrons scatter not more than once within the sample), extracting phase information from the Fourier transform of the measured images is relatively straightforward.

The lattice can be enhanced by Wiener filtering. Knowledge of the lattice parameters is not required for this procedure. Hence, the outcome is not biased by any imposed lattice parameters, which is an advantage.
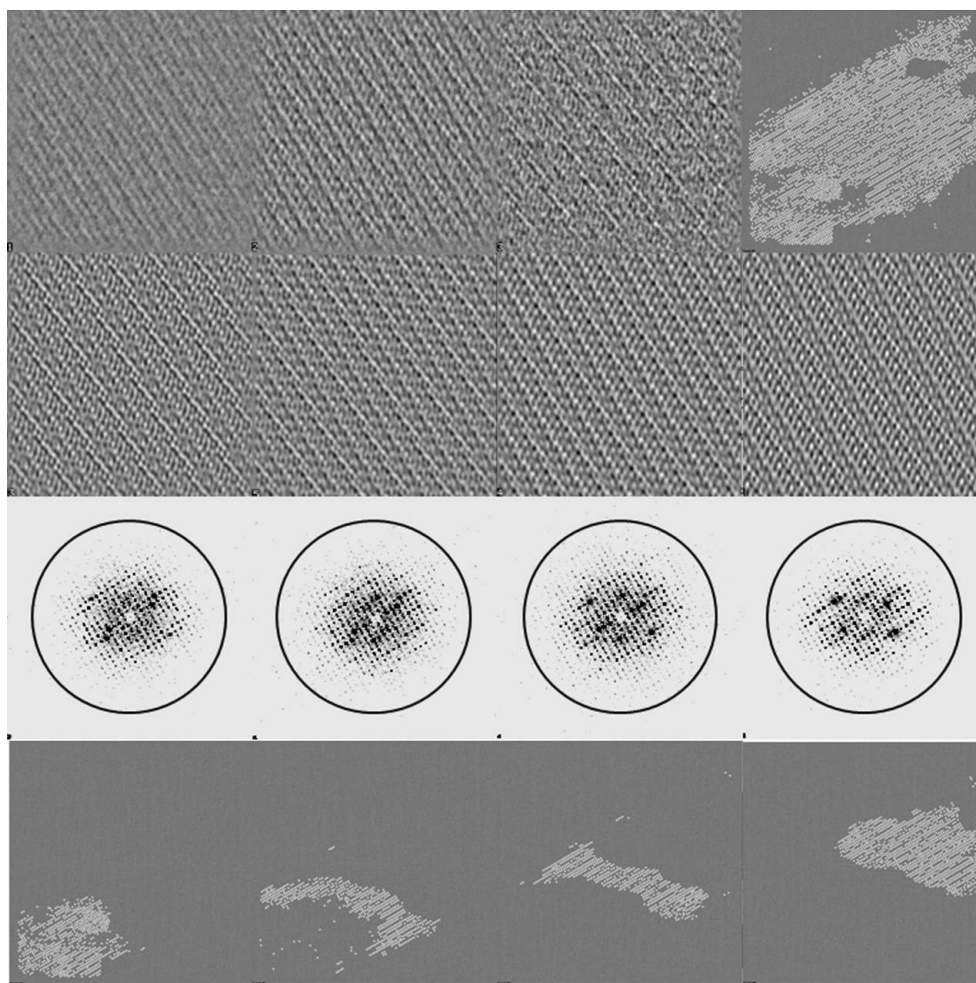

Figure 7
The top row of images shows the reconstructed projection classes of the electron image of the three-dimensional nanocrystal of lysozyme shown in Fig. 2 using just 101 non-overlapping sub-images (patches) of 256 × 256 pixels randomly selected from the Wiener-filtered image shown in Fig. 2. Using these three initial projection classes, we selected high-correlation patches; their locations are shown on the top right. These patches were classified into five classes, four of which are shown in the second panel from the top. The patches that contributed to each of these classes are located at the positions plotted in the bottom row. Patches were cut out of the original non-filtered image (Fig. 2a) at exactly the same locations and were assigned their corresponding shift and class parameters. The second panel from the bottom shows the amplitudes of the Fourier transforms of their class averages at low contour level and suggests a resolution of beyond 2 Å (the resolution of the circle is 2.1 Å and there are lattice spots well beyond this circle).

Using software designed for single-particle cryo-EM data analysis, the contrast and resolution of the projection images can be dramatically improved by identifying coherent domains of the crystals and averaging within them. With a similar aim, images of two-dimensional crystals have been analysed in the past using multivariate statistical analysis (MSA) in order to analyse the differences between adjacent unit cells in the two-dimensional lattice (Sherman *et al.*, 1998; Koeck *et al.*, 2007; Zeng *et al.*, 2007). However, here we analyse three-dimensional nanocrystals, which have some distinguishing differences compared with two-dimensional crystals. Since the third cell axis of the crystals is usually not aligned with the electron beam, the projection images usually show moiré patterns (see Fig. 2), which manifest themselves in the Fourier transform as multiple reciprocal two-dimensional lattices (Figs. 3 and 7). Note that the moiré unit repeat in the electron projection is larger than the projection of a single three-dimensional unit cell.

When crystals are also ordered in the third dimension they are less likely to be affected by warping and bending, or by in-plane rotations of the unit cell, because of increased crystal contacts. This will increase the probability of achieving high resolution. The increased thickness of the crystals will cause more pronounced dynamical scattering and a different defocus at the top and bottom of the crystal.

Detailed analysis revealed that within a crystal, we could observe different views of projected density within a single crystal, correlating with the location within the image (*cf.* Fig. 7). Potential causes are the following.

(i) The presence of mosaic blocks within the crystal, each with a slightly different orientation of the unit cells, resulting in different Bragg spots to be sliced by the Ewald sphere.

(ii) The crystal is not normal to the electron beam, resulting in a different focus for different parts of the crystal.

(iii) The crystal is not uniformly thick, resulting in a higher degree of dynamical scattering in the thicker parts of the crystal compared with the thinner parts.

Differential defocus is a less likely explanation of the observed differences, as this reduces the intensity of the Bragg spots in the reverse Fourier transforms uniformly within a resolution shell (provided that the microscope is stigmatically aligned). Fig. 7 does not suggest this to be the case. Differences in thickness of the crystal would result in a (subtle) density gradient of the image owing to increased electron absorption by thicker parts of the crystal. We did not observe such gradients. Furthermore, increased dynamical scattering can only cause the intensities of spots to become more alike, and we observe some spots that are present in one reverse transform to be absent in the other and *vice versa*, which cannot be explained by dynamical scattering effects. Hence, for the moment we consider the presence of mosaic blocks to be the most likely explanation of the observed differences. Macromolecular X-ray crystallography explicitly assumes and models the presence of such mosaic blocks within crystals; here, we could be seeing them directly for the first time.

Essential steps towards real space three-dimensional nanocrystallography have been taken. Next, we aim to automate the data analysis, so that projection views of many different orientations can be straightforwardly determined. We have made progress in this respect, as shown in Fig. 7. We also aim to apply three-dimensional reconstruction techniques that are well known in the single-particle cryo-EM community to the reconstruction of the three-dimensional crystal structure, initially at low resolution. However, at the resolution that we can now achieve (Fig. 7) we will also have to take aspects into account that single-particle analysis has so far been able to ignore: dynamical scattering and focal differences between the top and the bottom of the sample (equivalent to considering Ewald sphere curvature).
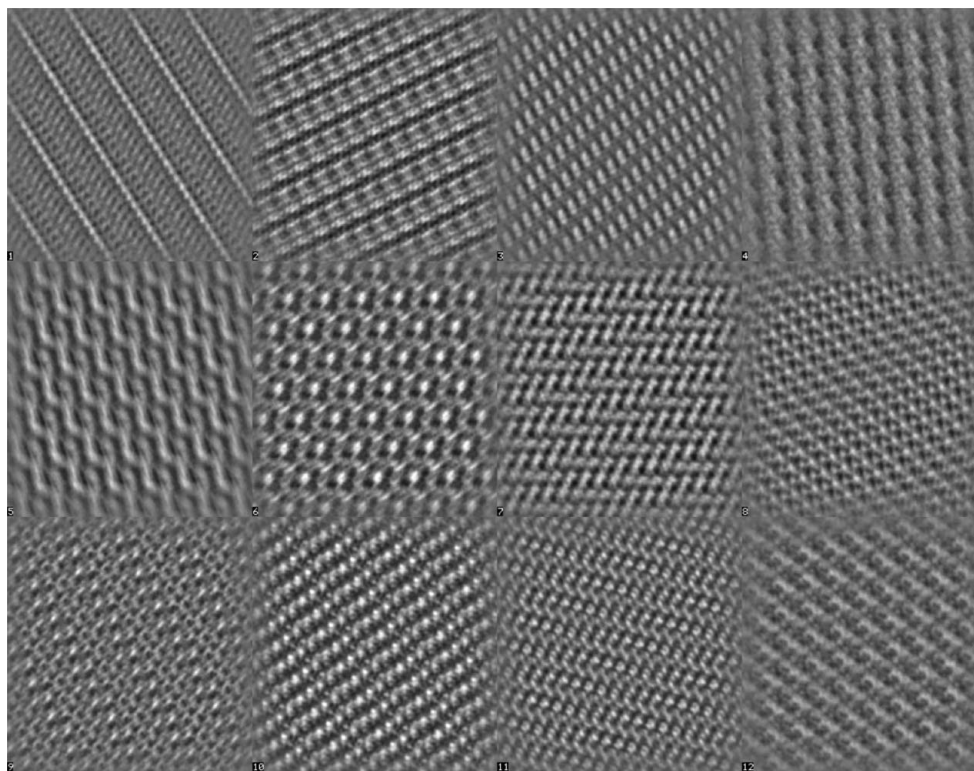
In subsequent refinement procedures with the aim of

Figure 8
A dozen of the more than 200 high-resolution projection images (resolution better than 2.5 Å judging from their Fourier transforms) of different lysozyme three-dimensional nanocrystals, all in different orientations. The data were collected as in Fig. 2 and processed as described in the text.

achieving high (atomic) resolution, these aspects will also have to be modelled. We assume that the knowledge that we obtain in this venture will assist in the field of single-particle analysis for analyzing structures of noncrystalline materials to resolutions at which these aspects can no longer be ignored.

References

Abramoff, M. D., Magelhaes, P. J. & Ram, S. J. (2004). *Biophotonics Int.* **11**, 36–42.

Carragher, B., Kisseberth, N., Kriegman, D., Milligan, R. A., Potter, C. S., Pulokas, J. & Reilein, A. (2000). *J. Struct. Biol.* **132**, 33–45.

Chapman, H. N. *et al.* (2011). *Nature (London)*, **470**, 73–77.

Cusack, S., Belrhali, H., Bram, A., Burghammer, M., Perrakis, A. & Riekel, C. (1998). *Nature Struct. Mol. Biol.* **5**, 634–637.

Dodson, E. J. (2001). *Acta Cryst.* D**57**, 1405–1409.

Eikenberry, E. F., Brönnimann, C., Hülsen, G., Toyokawa, H., Horisberger, R., Schmitt, B., Schulze-Briese, C. & Tomizaki, T. (2003). *Nucl. Instrum. Methods Phys. Res. A*, **501**, 260–266.

Frederik, P. M. & Hubert, D. H. W. (2005). *Methods Enzymol.* **391**, 431–448.

Gonen, T., Cheng, Y., Sliz, P., Hiroaki, Y., Fujiyoshi, Y., Harrison, S. C. & Walz, T. (2005). *Nature (London)*, **438**, 633–638.

Heel, M. van (1989). *Optik*, **82**, 114–126.

Heel, M. van, Gowen, B., Matadeen, R., Orlova, E. V., Finn, R., Pape, T., Cohen, D., Stark, H., Schmidt, R., Schatz, M. & Patwardhan, A. (2000). *Q. Rev. Biophys.* **33**, 307–369.

Heel, M. van, Harauz, G., Orlova, E. V., Schmidt, R. & Schatz, M. (1996). *J. Struct. Biol.* **116**, 17–24.

Heel, M. van, Portugal, R., Rohou, A., Linnemayr, C., Bebeacua, C., Schmidt, R., Grant, T. & Schatz, M. (2012). *International Tables for Crystallography*, Vol. *F*, 2nd online ed., edited by E. Arnold, D. M. Himmel & M. G. Rossmann, pp. 624–628. Chester: IUCr.

Henderson, R. (1995). *Q. Rev. Biophys.* **28**, 171–193.

Henderson, R. & Unwin, P. N. (1975). *Nature (London)*, **257**, 28–32.

Hohenstein, M. (1992). *Appl. Phys. Mater. Sci. Process.* **54**, 485–492.

Jansen, J., Tang, D., Zandbergen, H. W. & Schenk, H. (1998). *Acta Cryst.* A**54**, 91–101.

Klug, A. (1979). *Chem. Scr.* **14**, 245–256.

Knapek, E. & Dubochet, J. (1980). *J. Mol. Biol.* **141**, 147–161.

Koeck, P. J., Purhonen, P., Alvang, R., Grundberg, B. & Hebert, H. (2007). *J. Struct. Biol.* **160**, 344–352.

Kolb, U., Gorelik, T., Kübel, C., Otten, M. T. & Hubert, D. (2007). *Ultramicroscopy*, **107**, 507–513.

Llopart Cudié, X., Campbell, M., Dinapoli, R., San Segundo, D. & Pernigotti, E. (2002). *IEEE Trans. Nucl. Sci.* **49**, 2279–2283.

Mugnaioli, E., Gorelik, T. & Kolb, U. (2009). *Ultramicroscopy*, **109**, 758–765.

Navaza, J. (2008). *Acta Cryst.* D**64**, 70–75.

Nederlof, I., Van Genderen, E., Li, Y.-W. & Abrahams, J. P. (2013). Submitted.

Oleynikov, P., Hovmöller, S. & Zou, X. D. (2007). *Ultramicroscopy*, **107**, 523–533.

Philippsen, A., Engel, H. A. & Engel, A. (2007). *Ultramicroscopy*, **107**, 202–212.

Press, W. H., Teukolsky, S. A., Vetterling, W. T. & Flannery, B. P. (2007). *Numerical Recipes 3rd Edition: The Art of Scientific Computing*. Cambridge University Press.

Quevillon-Cheruel, S., Liger, D., Leulliot, N., Graille, M., Poupon, A., Li de La Sierra-Gallay, I., Zhou, C.-Z., Collinet, B., Janin, J. & Van Tilbeurgh, H. (2004). *Biochimie*, **86**, 617–623.

Rupp, B. (2004). *Protein Crystallization Strategies for Structural Genomics*, edited by N. Chayen, pp. 9–56. La Jolla: International University Line.

Sherman, M. B., Soejima, T., Chiu, W. & van Heel, M. (1998). *Ultramicroscopy*, **74**, 179–199.

Spence, J. C. H. & Zuo, J. M. (1992). *Electron Microdiffraction*. New York: Plenum.

Tang, G., Peng, L., Baldwin, P. R., Mann, D. S., Jiang, W., Rees, I. & Ludtke, S. J. (2007). *J. Struct. Biol.* **157**, 38–46.

Taylor, K. A. & Glaeser, R. M. (1974). *Science*, **186**, 1036–1037.

Tsuda, K. & Tanaka, M. (1995). *Acta Cryst.* A**51**, 7–19.

Vincent, R. & Midgley, P. (1994). *Ultramicroscopy*, **53**, 271–282.

Weirich, T. E., Zou, X. D., Ramlau, R., Simon, A., Cascarano, G. L., Giacovazzo, C. & Hovmöller, S. (2000). *Acta Cryst.* A**56**, 29–35.

Wolf, M., DeRosier, D. J. & Grigorieff, N. (2006). *Ultramicroscopy*, **106**, 376–382.

Zeng, X., Stahlberg, H. & Grigorieff, N. (2007). *J. Struct. Biol.* **160**, 362–374.

Zhang, D., Oleynikov, P., Hovmöller, S. & Zou, X. (2010). *Z. Kristallogr.* **225**, 94–102.

Zhou, Z. H. (2008). *Curr. Opin. Struct. Biol.* **18**, 218–228.

Zuo, J. & Spence, J. (1991). *Ultramicroscopy*, **35**, 185–196.